Check for updates

TECHNICAL ARTICLE

In Situ Micropillar Compression Tests of 304 Stainless Steels After Ion Irradiation and Helium Implantation

RYAN SCHOELL, 1 DAVID FRAZER, 2 CE ZHENG, 1 PETER HOSEMANN, 3 and DJAMEL KAOUMI 1,4

Department of Nuclear Engineering, North Carolina State University, Raleigh, NC 27607, USA.
 Los Alamos National Laboratory, Los Alamos, NM 87544, USA.
 Department of Nuclear Engineering, University of California, Berkeley, CA 94720, USA.
 dkaoumi@ncsu.edu

A study was conducted to better understand the roles of irradiation defects and cavities on the mechanical properties of 304 stainless steel. Micropillars were fabricated using focused ion beam techniques, and pillars were heat treated at 300°C to serve as a control, irradiated in situ to 5 dpa with 1 MeV krypton ions at 300°C, or pre-implanted with a specific amount of helium and then irradiated. Micropillars were compression tested in situ in a transmission electron microscope (TEM) using a picoindenter. The load–displacement curves were converted into stress–strain curves and mechanical properties were extracted. Irradiation hardening was observed with the yield stress being the highest in the pillar implanted with the least helium. TEM and energy-dispersive spectroscopy analysis showed the presence of irradiation-induced defects in krypton-irradiated samples and the presence of cavities.

INTRODUCTION

In a nuclear reactor, various structural components around the nuclear core are fabricated out of austenitic stainless steel (SS) 304. These components include the bolts that are used to hold core internals. Being so close to the core, these 304 components are subjected to both neutron irradiation as well as helium generation from alpha decay and transmutation.² The process of neutron irradiation causing damage and helium generation can alter the mechanical properties of the component. Specifically, hardening and embrittlement are often observed in irradiated 304.3 It is has been found that helium is insoluble in many reactor component materials and often precipitates out to form clusters and bubbles. Helium implantation and generation in reactor components have been shown to alter the mechanical properties of the components and can lead to brittle facture around grain boundaries. 1,4,5 To gain a better understanding of the effects of irradiation and helium implantations on the mechanical properties, in situ micropillar tests were conducted. The benefit of micropillar testing is the ability to observe how the microstructural changes from irradiation and implantation alter the mechanical properties. Additionally, the change in

the microstructure upon deformation in a transmission electron microscope (TEM) offers the ability to see how the microstructural changes react to deformation. Many studies involving irradiation and/or helium implantation use some version of a hardness test to quantify the hardness of the material before and after irradiation. ^{2,6–10} Although this technique is adequate to capture the hardness that can be used to estimate the yield strength, the test often lacks the ability to show the deformation of the new microstructure. Ion irradiation is a useful tool to simulate neutron damage in materials. The use of ions allows for fine control over the flux and energy as well as the ion species. Additionally, samples do not need to be analyzed in a hot cell because no radioactive species are forming like those that form under neutron irradiation. Unfortunately, ion irradiation damage is usually only limited to a small depth into the structural metals used in reactors compared with neutron irradiation.³ Fortunately, micromechanical testing is well suited to ion irradiation studies since the thickness of the material used is on the same order. The goal of the study is to investigate how micromechanical testing can offer a better comprehension of ion irradiation as well as helium implantation on the mechanical properties of 304.

MATERIALS AND METHODS

A sample of commercial stainless steel 304 (nominal wt.% < 0.08% C, 17.5e20%Cr, 8e11%, < 2% Mn, < 1% Si, < 0.045% P, and < 0.03% S) from the same piece as published previously 3,11,12 was obtained and engineered into micropillars for compression testing. Micropillars were fabricated with the aid of a dual-beam FEI Quanta focused ion beam (FIB) and field-emission scanning electron microscope (SEM). The FIB was used to shape the pillars to a shape of approximately 300 nm wide and 500 nm tall. The pillars that were not irradiated with helium or krypton ions underwent a heat treatment under the vacuum of an SEM where the samples were heated to 300°C in 11 min and then held at 300°C for 3 h 50 min. The other pillars were at 300°C for about the same duration during krypton ion irradiation. To compress each pillar, a Hysitron PI-95 TEM picoindenter was used in a JEOL 3010 microscope at the National Center for Electron Microscopy (NCEM). The PI-95 can track the displacement as well as the load on the pillars during compression in situ in the TEM. Put in displacement control, the PI-95 1 μm flat tip was set to a displacement rate of 7 nm/s, which corresponds to a strain rate of $1.4 \times 10^{-2} \, \mathrm{s}^{-1}$ and was compressed along the height of the pillar. Before the pillar compressions, several of the pillars were irradiated with 1-MeV krypton ions at $300^{\circ}\text{C} \pm 3^{\circ}\text{C}$ with a flux of $6.25\times 10^{11}\frac{\dot{s}_{\rm ions}}{cm^2s}$ at an angle of 15° from the normal of the front face of the pillar until the sample reached a dose of 5 dpa. Heating due to ion irradiation was estimated to be around 20-30 K. According to the SRIM-2008 simulation shown in Fig. 1, in the material thickness, there is a relatively uniform damage profile of about 5 dpa.

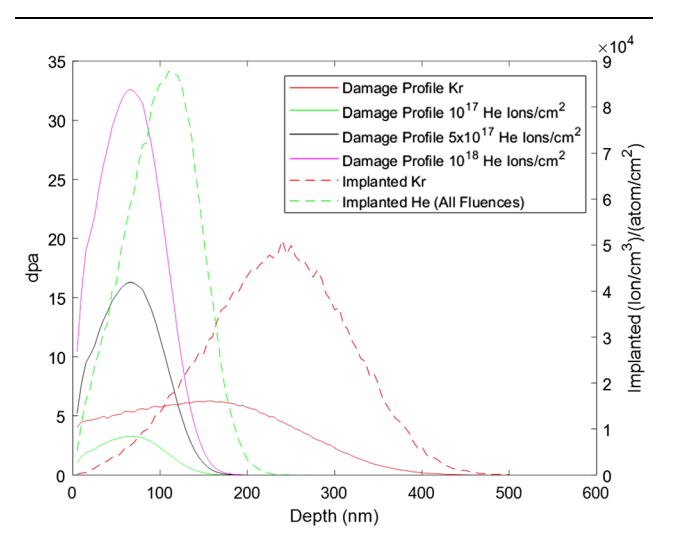


Fig. 1. Damage profile of 1-MeV Kr ion irradiations and 25-keV He Ion and Kr and He ion distribution in the 304SS was calculated with SRIM-2008 using the quick damage mode with average displacement energies of 40, and 28 eV for metallic and non-metallic atoms, respectively.

Additionally, the damage profile for 25 keV helium suggests an average damage of 1.09 ×10⁻² vacancies/ion/Å over the thickness of the pillar, which translates into 1.24, 6.22, and 12.44 dpa for the helium fluences of 1×10^{17} , 5×10^{17} , and 1×10^{18} He⁺ ion/cm², respectively. The implantation of both helium and krypton ions into the material is also evident in Fig. 1. The 300-nm-thick pillars will retain most of the helium implanted into them, while a large portion of krypton ions will also be implanted. The ion irradiation was performed in situ at the Intermediate Voltage Electron Microscope (IVEM) facility at Argonne National Laboratory with their Hitachi 9000NAR TEM operating at 300 keV. Videos of the irradiation were recorded at a rate of 25 frames per second, and TEM micrographs of one of the pillars was obtained at 0, 0.1, 0.3, 0.5, 0.7, 1, 2, 3, 4, and 5 dpa to track the evolution of the microstructure. The videos were used to perform frame-by-frame analysis to better observe the dynamic microstructure evolution. Other pillars were implanted with helium to fluences of 1×10^{17} , 5×10^{17} , and 1×10^{18} He⁺ ion/cm² followed by Kr ion irradiation to 5 dpa. The helium implantation was performed at the University of California Berkeley using 25-keV helium ions in the Orion NanoFab Helium Ion Beam Microscope (HIM). The helium implantation was done normal to the front-facing side of the pillar, and the converged helium beam was set to raster over the area of the pillar until a specific fluence was reached. The experimental conditions are shown in Table I.

The forces during extension of the 1- μ m flat tip were used to calculate stresses at specific strains of the material to develop stress-strain curves. The curves were then used to the obtain mechanical properties of each pillar such as the yield stress to understand how ion irradiation affects the mechanical properties. Furthermore, to understand why the mechanical properties varied, a look into the microstructure was carried out by further characterizing each pillar using a probe aberration-corrected field emission FEI Titan TEM equipped with a SuperX energy dispersive spectroscopy (EDS) system at the Analytical Instrument Facility (AIF) at North Carolina State University to obtain chemical maps of the pillars. Additionally, irradiation damage in the form of clusters, segregation, and/or cavities was analyzed in the samples that were subjected to ion irradiation.

RESULTS

The stress-strain curves of the different pillar conditions are shown below in Fig. 2a. The plastic flow evident in the stress-strain curve shows load drops, especially the curves belonging to the helium-implanted pillars. From the stress-strain curves, an obvious shift in the curves from the control pillars to the 5-dpa pillars to the helium-implanted pillars is

Table I. Experimental conditions for 304SS pillars	pillars			
Experiment	Temperature	Number of pillars	Fluence	Displacements per atom
Control Kr ion irradiation to 5 dpa	300°C heat treatment 300°C during Kr irradiation	5 3	$2.89 imes 10^{15} rac{\mathrm{Kr\ ions}}{\mathrm{cm}^2}$	_ 5 dpa
Helium implantation 1×10^{17} ion/cm 2 followed by Kr irradiation to 5 dna	300°C during Kr irradiation	23	$1 imes 10^{17} rac{ m He\ ions}{ m cm^2}$	1.24~ m dpa~He~and~5~dpa~Kr
Helium implantation $5_T = 10^{17}$ ion/cm ² followed by Kr Irradiation to 5 dna	300°C during Kr irradiation	23	$5 imes 10^{17} rac{\mathrm{He~ions}}{\mathrm{cm}^2}$	$6.22~\mathrm{dpa}$ He and $5~\mathrm{dpa}$ Kr
Helium implantation 1×10^{18} ion/cm ² followed by Kr irradiation to 5 dpa	300°C during Kr irradiation	Ø	$1\times 10^{18} \frac{\rm He~ions}{\rm cm^2}$	12.44 dpa He and 5 dpa Kr

obvious. Mechanical properties such as the flow stress at 5% strain were obtained from the stressstrain curves and are evident in Fig. 2b and d, respectively. The flow stress at 5% strain was used since there can be some ambiguity related to the yield stress of micropillars. The flow stress at 5% strain for the helium-implanted pillars shows that the highest flow stress belongs to the pillar implanted with the least amount of helium. Moreover, the flow stress appears to decrease with increasing implanted helium. The orientations of the Kr-irradiated pillars only and the helium-implanted pillars relative to the compression axis were found to be about 11° and 21° from the [111] direction, respectively. With the known orientation, critical resolved shear stress (CRSS) plots were generated and are shown in Fig. 2c.

To gain a better understanding of why the mechanical properties of 304 were altered by irradiation, a detailed look into the microstructure was carried out. Before compressing, one of the pillars that was just irradiated to 5 dpa with no helium implantation was followed during irradiation in situ. The pillar was tilted to a weak beam condition along the (111) family of reflections to observe radiation damage. Bright-field (BF) TEM micrographs of the pillar are shown in Fig. 3 and were obtained at different doses. The micrographs show that clusters of irradiation-induced defects have formed and also disappear. From the frame-byframe analysis of the videos, irradiation-induced defects were evident as early as about 0.009 dpa. The defect population over the duration of irradiation appears to have grown in size and shrunk in number density. This is most evident when comparing the micrograph at 5 dpa to the micrograph at 0.1 dpa where the latter has small dark spots around the area and the former only has large defects in localized areas. Chemical maps before and after irradiation on the same pillar were used to identify any segregation of elements using the scanning transmission electron microscopy's (STEM) energy-dispersive spectroscopy (EDS) system known as ChemiSTEM. From the chemical maps there was no evidence of chemical segregation. The small size of the pillars relative to the size of a single grain of 304 led to pillars being essentially single crystals. It has been shown that austenitic stainless steels can undergo radiationinduced segregation (RIS) at the grain boundaries but it is not expected to play a role in this experiment because of the lack of grain boundaries. 13,14 Additionally, from the chemical maps there appears to be no evidence of any large cavities after irradiation.

Following the microstructural characterization, the helium-implanted samples were also observed under the TEM before and after Kr ion irradiation. Before Kr irradiation, Fresnel imaging techniques were applied to the pillars implanted with various amounts of helium to detect any voids that may

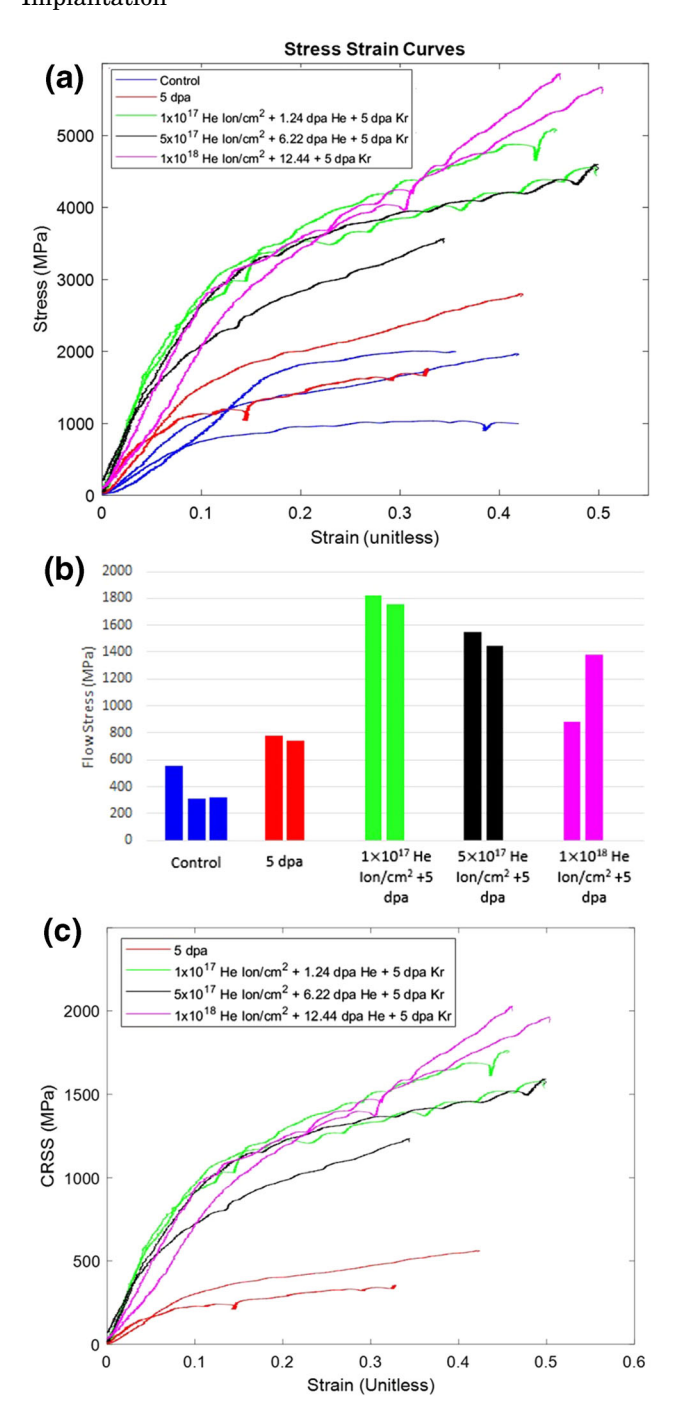


Fig. 2. (a) Stress–strain curves, (b) flow stress at 5% strain for the various 304SS pillars, and (c) critical resolved shear stress.

have formed from helium implantation alone. Formation of cavities for the pillars subjected to 10^{18} He ions/cm² can be seen in Fig. 4a. These cavities appear to be spherical in nature and not faceted. Cavities were not detected in either of the lower helium implanted fluencies. After irradiation, the voids for the 10^{18} He ions/cm² appear to grow in size and number density as shown at various doses in Fig. 4a. Figure 4b and c shows the nucleation and growth in cavities for the pillars with 10^{17} He ions/cm² and 5×10^{17} He ions/cm², respectively.

Nucleation for both lower fluence helium-implanted pillars was observed around 1.12×10^{15} Kr ions/ cm². Further analysis into the microstructure of the helium-implanted pillars with 5 dpa of irradiation damage was conducted using the SuperX EDS system to obtain chemical maps. Chemical maps of a region on the 10^{18} He ion/cm² that contained cavities is shown in Fig. 5a. From the micrograph, the cavities appear to be spherical with a 1.5–6 nm range of diameters. The chemical maps all show areas depleted in each of the elements in the regions where the cavities are as shown by the arrow. Unfortunately, the EDS method is limited by the fact that helium maps cannot be obtained and techniques such as electron energy loss spectroscopy (EELS) would have to be used to identify helium via its k-edge at 22 eV; however, the pillars are too thick and put the helium edge in the plasmon region making the spectrum around 22 eV convoluted. Figure 5b and c for 10^{17} He ion/cm² and 5×10^{17} He ion/cm², respectively, shows a similar depletion of elements in the chemical maps and an EDS spectrum that shows the decrease in the counts of each element indicating cavities. The sizes and number density of the 10^{17} He ion/cm² and 5×10^{17} He ion/cm² appear to be smaller compared with the 10¹⁸ He ion/cm² pillar. Besides cavities, clusters of irradiation-induced damage were observed using dark-field imaging in various reflection directions as shown in Fig. 6.

After the microstructure of the pillars had been analyzed, the pillar compression tests were conducted in situ under TEM observations. Videos of the pillar's compression were obtained (videos are uploaded as supporting documents) and snap shots at various strains were taken and can be found in the electronic references.

DISCUSSION

The changes in the microstructure from helium implantation and Kr ion irradiation can be used to explain the changes in the mechanical properties obtained from the pillar compression test. It should be noted that the control pillars, 5 dpa pillars, and helium-implanted pillars all had different orientations relative to the compression axis. The average grain size for 304SS is on the order of about 30-40 μ m so pillars of the same group tended to have the same crystallographic orientation relative to the compression axis. Moreover, each pillar can be treated as a single crystal. The grain orientation can have an effect on the mechanical properties and should be taken into account. From Fig. 3, the pillars only irradiated to 5 dpa with no helium implantation had a compression axis 11.8° from the [111] direction. Likewise, the pillars implanted with helium had a similar orientation as shown in Fig. 6.

The engineering stress-strain curves for the helium-implanted and krypton-irradiated sample show load drops under plastic flow. Other

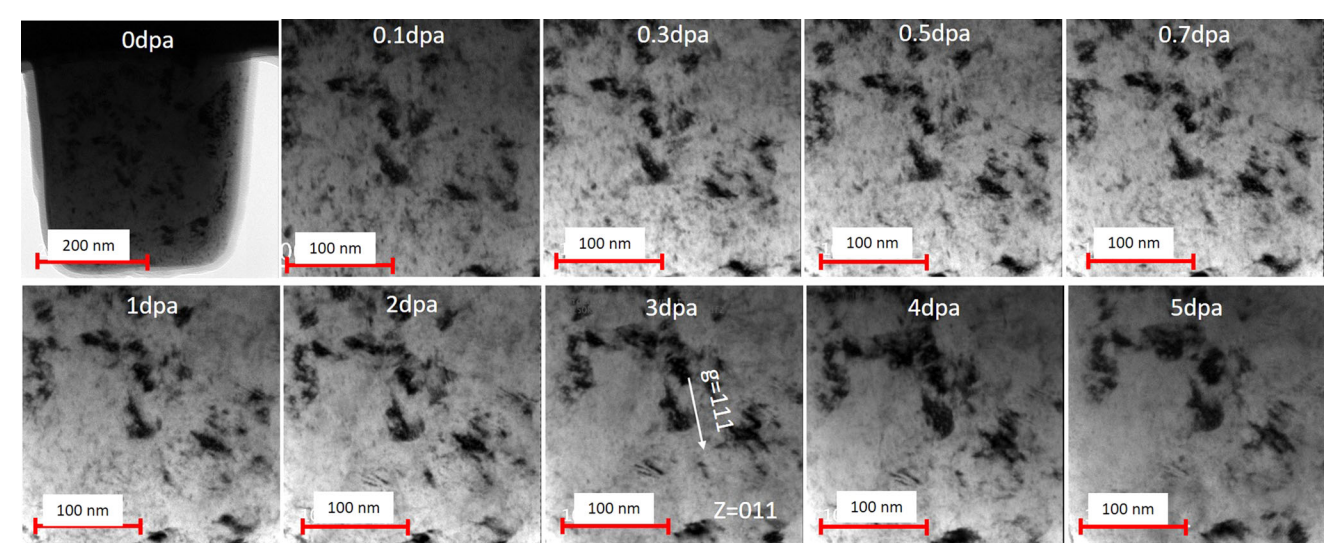


Fig. 3. BF TEM micrographs of 304 pillar at 300°C at various doses under Kr irradiation.

researchers have reported in ^{15,16} serrations in unirradiated nickel-based micropillar stress—strain curves resulting from the stochastic nature of the plastic flow due to the small volume of material; however, no serrations were evident in the control pillars. Load drops in the plastic flow curve were evident in both the helium-implanted pillars and the pillars that were only irradiated with krypton ions. Defect-free channels have been suggested to occur at high doses of 25 dpa in nickel from dislocation-created defects reacting with one another ¹⁶

From the microstructure, the addition of irradiation-induced defects clearly added features to the microstructure that hindered dislocation motion. As a result of hindered dislocation motion, an increase in the flow stress of the irradiated pillars is seen compared with the control known as irradiation hardening. Comparing the microstructure of the pillars with no implanted helium with those that were, the addition of cavities and helium solutes as well as irradiation-induced defects clearly is more effective in hindering dislocation motion as shown as an increase in flow stress. 17 The 10^{18} He ion/cm 2 pillars showed signs of cavities even before krypton ion irradiation. Reports of no signs of cavities after only helium implantation except at high fluences have been reported. Although cavities are considered weak obstacles to dislocations, they still managed to increase the flow stress significantly compared with just the krypton irradiation case. Several researchers have also reported the increase in the yield strength after ion irradiation. ^{1–3}

Many researchers have attributed the increase in yield strength from helium bubbles to the interaction between gliding dislocations and the bubbles. ^{1,18} The bubbles act as obstacles to gliding

dislocation, which bows the dislocation, and a higher stress is needed to continue plastic deformation. ¹⁸ One model that can be used to elucidate the hardening caused by helium bubbles is known as the Friedel-Kroupa-Hirsch (FHK) hardening model ^{18,19}:

$$\Delta\sigma=rac{1}{8}M\mu bdN_{
m bubbles}^{rac{2}{3}}$$

where $\Delta \sigma$ is the change in yield strength, M is the Taylor factor (3.06 for FCC ¹⁷), μ is the shear modulus, b is the Burgers vector, d is the diameter of a bubble, and $N_{\rm bubble}$ is the number density of bubbles in the sample. To calculate the bubble density, one can use a pressure-based method that is used elsewhere ^{18,20}:

$$p = \frac{2\gamma + \mu b}{r}$$

where p is the pressure inside the bubble, γ is the surface energy, which was taken to be 1.65 J/m² for the (111) orientation, 21 μ is the shear stress taken to be 72 GPa, 22 b is the Burgers vector of γ -Fe in the [110](111) slip system, and r is the radius of the bubbles. To calculate the radius of the bubbles, STEM high-angle annular dark-field (HAADF) images were used for the samples implanted with helium. Although the bubbles are assumed to be circular in nature, they were found to be ellipses. An equivalent diameter was calculated using the following:

$$d_{eq} = \sqrt{a imes b}$$

where a and b are the lengths of the major and minor axis, respectively. The average diameter for the $1\times 10^{17} \frac{\text{He ion}}{\text{cm}^2}$, $5\times 10^{17} \frac{\text{He ion}}{\text{cm}^2}$, and $1\times 10^{18} \frac{\text{He ion}}{\text{cm}^2}$

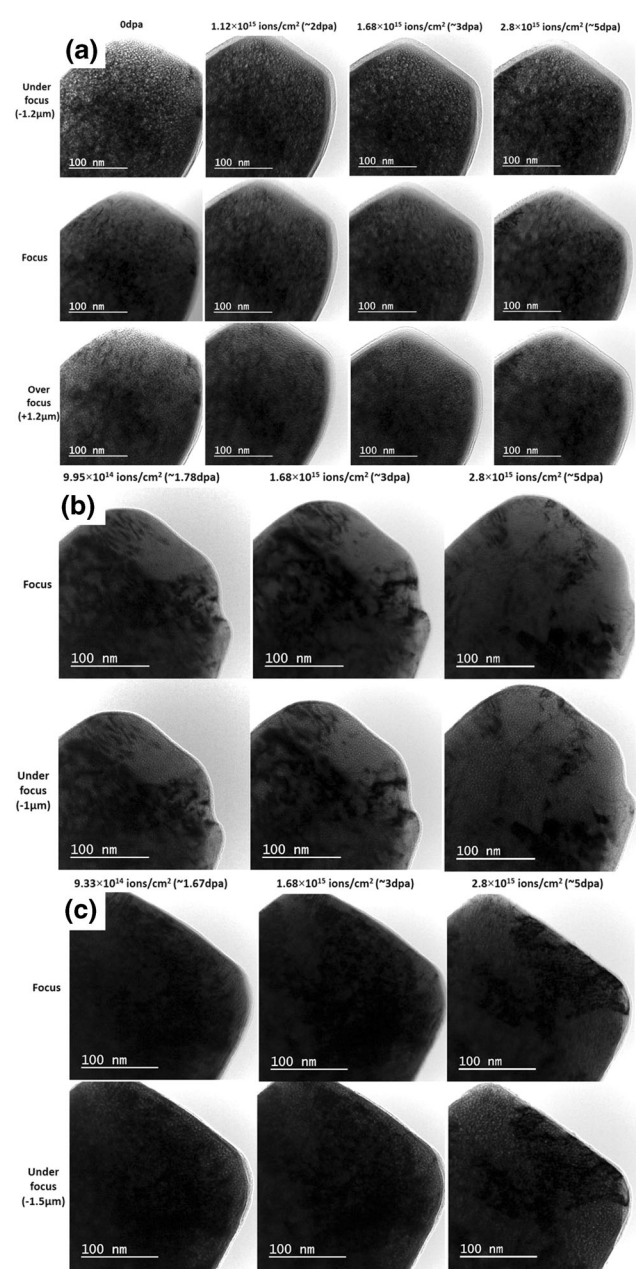


Fig. 4. Fresnel imaging of helium-implanted pillars at various Kr doses for the (a) $1\times10^{18}\frac{\text{He ion}}{\text{cm}^2},$ (b) $1\times10^{17}\frac{\text{He ion}}{\text{cm}^2},$ and (c) $5\times10^{17}\frac{\text{He ion}}{\text{cm}^2}.$

were 1.88 nm, 2.25 nm, and 4.12 nm, respectively. Converting the diameters to radii, the pressure inside the bubbles was found to be 23.1 GPa, 19.4 GPa, and 10.6 GPa for the $1\times10^{17}\frac{\text{He ion}}{\text{cm}^2}$, $5\times10^{17}\frac{\text{He ion}}{\text{cm}^2}$, and $1\times10^{18}\frac{\text{He ion}}{\text{cm}^2}$ pillars, respectively. The molar volume of helium inside the pillars using the ideal gas law ¹⁸ was then calculated for each case. The molar volume combined with the volume of the average bubble was used to calculate the number of helium atoms per bubble, N_{He} . The number density of bubbles was then calculated using

$$N_{
m bubble} = rac{R_{
m He}N_{
m Fe}}{N_{
m He}}$$

where $R_{\rm He}$ is the atomic concentration of helium implanted and $N_{\rm Fe}$ is the atomic density of iron. It should be noted that all helium is assumed to be trapped only in bubbles. Comparing the calculated number density with the measured number density showed both were in good agreement. It should be noted that the helium bubble number density and size were performed around the center of the pillars. From the FHK model, the increase in hardening due to helium bubbles was calculated to be 40.8 MPa, for $1 \times 10^{17} \frac{\text{He ion}}{\text{cm}^2}$, 113 MPa, and 146 MPa $5 \times 10^{17} \frac{\text{He ion}}{\text{cm}^2}$, and $1 \times 10^{18} \frac{\text{He ion}}{\text{cm}^2}$ pillars, respectively. Comparing these predicted values with the difference in flow stress at 5% strain of the 5 dpaonly case and the helium-implanted case shows that the model under-predicts the increase in hardening. From this analysis, there appear to be other hardening mechanisms at play that have increased the vield strength further. Specifically, helium might not just be trapped in the bubbles but is also in the lattice. In fact, the amount of helium implanted into the material might be supersaturating the material meaning that the ideal gas law would not be able to hold. The implantation of helium into the 300-thick pillars was shown through the SRIM calculation to not be entirely uniform with most of the helium implanting around the first 100 nm into the pillar thickness. Additionally, from the implantation profile in Fig. 1, many krypton ions are also being implanted. These krypton ions might also be trapped within the lattice and leading to hardening of the material. The hardening coefficient used for the FHK model is 0.2 but other researchers have indicated that a higher coefficient might be needed when the helium bubble radius exceeds that of 2 nm. Other studies have found that hardening due to bubble formation only contributes to a fraction of hardening in 316 stainless steels.²³ Finally, the higher helium fluence contained more damage from the helium implantation; however, it has been shown elsewhere that an increase in yield strength of 304SS under neutron irradiation at temperatures of 418–450°C reaches saturation after about 5 dpa.²⁴

CONCLUSION

This study investigated the effects of irradiation as well as helium implantation on the mechanical properties of austenitic stainless steel 304. Micropillars were fabricated and were heat treated to serve as controls, irradiated with 1 MeV krypton ions at 300°C to 5 dpa, or pre-implanted with helium ions and then irradiated with 1 MeV krypton ions at 300°C to 5 dpa. The pillar compression tests tracked the load over displacement and was converted to a stress–strain curve. The yield stress was extracted and showed that the material hardened under

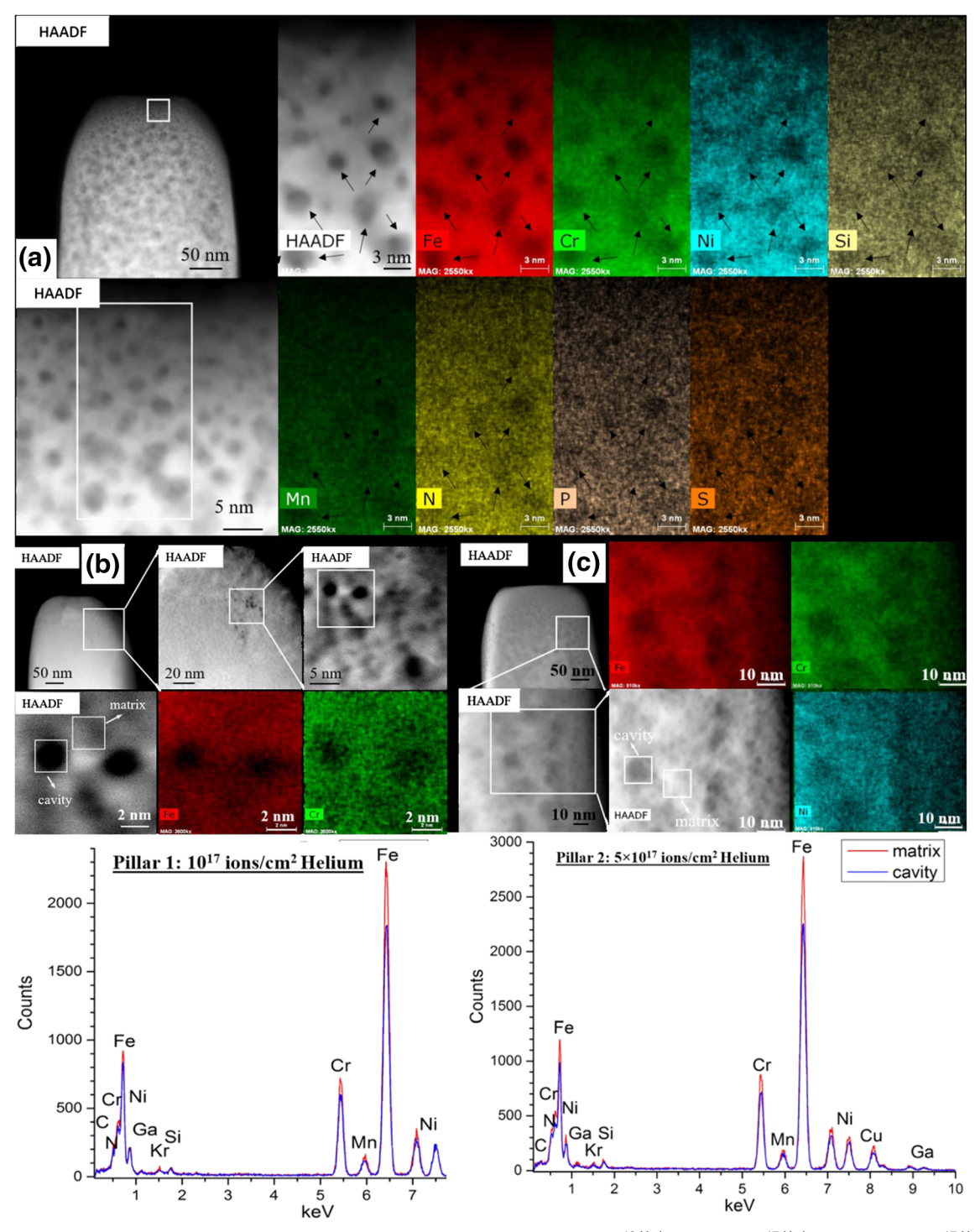


Fig. 5. Chemical maps from ChemiSTEM for helium pillars from a fluence of (a) $1 \times 10^{18} \frac{\text{He ion}}{\text{cm}^2}$, (b) $1 \times 10^{17} \frac{\text{He ion}}{\text{cm}^2}$, and (c) $5 \times 10^{17} \frac{\text{He ion}}{\text{cm}^2}$.

irradiation with the highest yield stress being the pillar implanted with the most helium. The microstructure through TEM and ChemiSTEM observation revealed irradiation damage in the form of loops and clusters as well as cavities in the pillar implanted with the least helium. The irradiation-induced defects as well as the cavities were the most effective in hindering dislocation motion,

effectively increasing the flow stress required to cause deformation. Using the Friedel–Kroupa–Hirsch model for quantifying the increase in hardness from helium bubbles suggests that other hardening mechanisms are at play. The implanted helium and krypton might also be stuck in the lattice and lead to further hardening. Additionally, the high fluence of helium implanted into the pillars

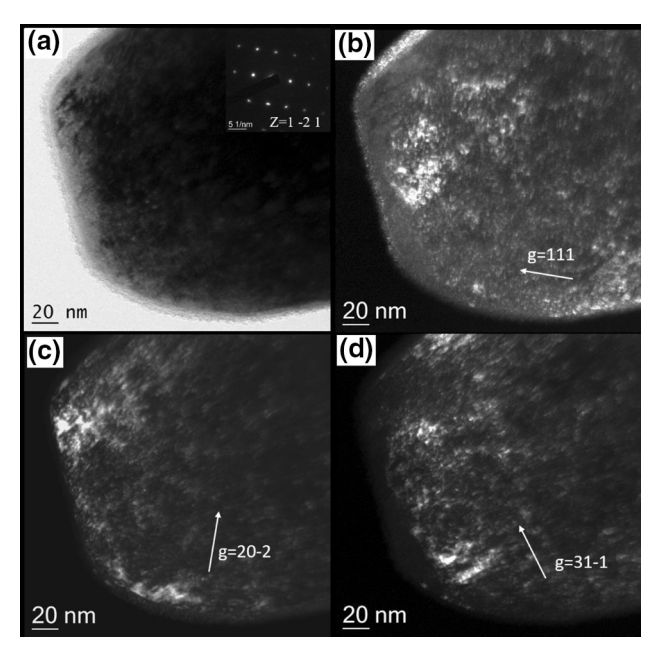


Fig. 6. Bright-field TEM micrograph taken at the zone axis [1-2 1]. Different diffraction vectors, (b) g=111, (c) g=20-2, and (d) g=31-1, were used to image the radiation-induced defects (black dots, dislocation and dislocation loops) in the pillar with 10^{18} helium/cm² in situ irradiated by 1 MeV krypton at 573 K at the dose of 2.8 \times 10^{15} ions/cm².

might have led to the supersaturation of helium into the pillar. Supersaturation of helium would indicate that the ideal gas law would not be valid. Finally, helium bubbles might only be increasing the hardness by a fraction of the total hardness.

ACKNOWLEDGEMENTS

This work was performed in part at the Analytical Instrumentation Facility (AIF) at North Carolina State University, supported by the State of North Carolina and the National Science Foundation (Award No. ECCS-1542015). The AIF is a member of the North Carolina Research Triangle Nanotechnology Network (RTNN), a site in the National Nanotechnology Coordinated Infrastructure (NNCI). The authors also acknowledge funding from NSFDMR Award No. 1807822. This work was partially performed at the National Center for Electron Microscopy, which is supported by the Office of Science, Office of Basic Energy Sciences, of the US Department of Energy under contract no. DE-AC02-05CH11231. The authors thank Pete

Baldo, Ed Ryan, Jing Hu, Meimei Li, and Mark Kirk at the IVEM facility for their assistance.

REFERENCES

- I. Villacampa, J.C. Chen, P. Spatig, H.P. Seifert, and F. Duval, J. Nucl. Mater. 500, 389 (2018).
- C. Heintze, F. Bergner, M. Hernandez-Mayoral, R. Kogler, G. Muller, and A. Ulbricht, J. Nucl. Mater. 470, 258 (2016).
- J. Weaver, S. Pathak, A. Reichardt, H. Vo, S. Maloy, P. Hosemann, and N. Mara, J. Nucl. Mater. 493, 368 (2017).
- Y. Katoh, M. Ando, and A. Kohyama, J. Nucl. Mater. 323, 251 (2003).
- J. Henry, M.H. Mathon, and P. Jung, J. Nucl. Mater. 318, 249 (2003).
- J. Gao, K. Yabuuchi, and A. Kimura, J. Nucl. Mater. 515, 294 (2019).
- M. Roldan, P. Fernandez, J. Rams, D. Jimenez-Rey, E. Materna-Morris, and M. Klimenkov, J. Nucl. Mater. 460, 226 (2015).
- F. Bergner, G. Hlawacek, and C. Heintze, J. Nucl. Mater. 505, 267 (2018).
- Y. Xin, X. Ju, J. Qiu, L. Guo, J. Chen, Z. Yang, P. Zhang, X. Cao, and B. Wang, Fusion Eng. Des. 87, 432 (2012).
- C.D. Judge, V. Bhakhri, Z. Jiao, R.J. Klassen, G. Was, G.A. Botton, M. Griffiths (2017).
- A. Reichardt, A. Lupinacci, D. Frazer, N. Bailey, H. Vo, C. Howard, Z. Jiao, A. Minor, P. Chou, and P. Hosemann, J. Nucl. Mater. 486, 323 (2017).
- H. Vo, A. Reichardt, D. Frazer, N. Bailey, P. Chou, and P. Hosemann, J. Nucl. Mater. 493, 336 (2017).
- K.G. Field, M.N. Gussev, and J.T. Busby, *Trans. Am. Nucl. Soc.* 110, 1025 (2014).
- 14. K. Nakata and I. Masaoka, J. Nucl. Mater. 150, 186 (1987).
- C.P. Frick, B.G. Clark, S. Orso, A.S. Schneider, and E. Arzt, *Mater. Sci. Eng.*, A 489, 319 (2008).
- X. Zhao, D. Strickland, P. Derlet, M. He, Y. Cheng, K. Hattar, and D. Gianola, Acta Mater. 88, 121 (2015).
- F. Zhu, D. Wang, N. Gao, H. Peng, Z. Xie, and Z. Zhang, J. Nucl. Mater. 518, 226 (2019).
- P. Landau, Q. Guo, P. Hosemann, Y. Wang, and J. Greer, *Mater. Sci. Eng.*, A 612, 316 (2014).
- N. Li, M.S. Martin, O. Anderoglu, A. Misra, L. Shao, H. Wang, and X. Zhang, J. Appl. Phys. (Melville, NY, USA) 105, 123522 (2009)
- J.A. Knapp, D.M. Follstaedt, and S.M. Myers, *J. Appl. Phys.* (*Melville*, *NY*, *US*) 103, 013518 (2008).
- 21. Z. Rak and D.W. Brenner, Appl. Surf. Sci. 402, 108 (2017).
- T. Jayakumar, A. Kumar, and B. Raj, AIP Conf. Proc. 975, 1162 (2008).
- M. Toloczko, G. Tedeski, G. Lucas, G. Odette, R. Stoller, and M. Hamilton, MRS Online Proc. Libr. 373, 207 (2011).
- E. Rabenberg, B. Jaques, B. Sencer, F. Garner, P. Freyer, T. Okita, and D. Butt, J. Nucl. Mater. 448, 315 (2014).

Publisher's Note Springer Nature remains neutral with regard to jurisdictional claims in published maps and institutional affiliations.